Rheological transition in simple shear of moderately dense assemblies of dry cohesive granules

Eric Murphy,[1] Sriram Sundararajan,[2] and Shankar Subramaniam[1,*]

[1]*Center for Multiphase Flow Research and Education, Department of Mechanical Engineering,*
Iowa State University, Ames, Iowa 50011, USA
[2]*Department of Mechanical Engineering, Iowa State University, Ames, Iowa 50011, USA*

The rheology of homogeneous cohesive granular assemblies under shear at moderate volume fractions is investigated using the discrete element method for both frictionless and frictional granules. A transition in rheology from inertial to quasistatic scaling is observed at volume fractions below the jamming point of noncohesive systems, which is a function of the granular temperature, energy dissipation, and cohesive potential. The transition is found to be the result of growing clusters, which eventually percolate the domain, and change the mode of momentum transport in the system. Differences in the behavior of the shear stress normalized by the pressure are observed when frictionless and frictional cases are compared. These differences are explained through contact anisotropy after percolation occurs. Both frictionless and frictional systems are found to be vulnerable to instabilities after full system percolation has occurred, where the former becomes thermodynamically unstable and the latter may form shear bands. Finally, implications for constitutive modeling are discussed.

I. INTRODUCTION

As the size of particles in a granular flow is decreased, reaching the μm size range, a number of phenomena appear that are otherwise unimportant for larger particles, e.g., millimeter sized. Cohesion in the form of van der Waals forces, liquid bridging, and long-ranged electrostatics become important. Repulsive electrostatics may also be present. The cohesive mechanisms cause a number of interesting differences in the characteristic flow behavior when compared to noncohesive systems. For example, a marked increase in yield stresses is observed in the presence of cohesion [1–5]. Additionally, in numerical experiments a quasistatic stress scaling, where shear stress does not depend on shear rate [6], is observed at volume fractions well below volume fractions characteristic of jamming for noncohesive systems [1,3]. Both of these effects have been observed to cause plug flows in gravity-driven chute flows of granular media, where the size of the plug grows with cohesion strength [7]. On the other hand, in split cell rheometers, cohesion is observed to increase the size of the shear band, decreasing the size of the static areas of the flow [8]. In this paper we attempt to explore some of the origins of these behaviors from a physics-based microscopic viewpoint, and elucidate some of the challenges in constitutive modeling of cohesive materials.

We focus primarily on dry cohesive systems with van der Waals cohesion. Systems where the effect of short-ranged cohesion is important are widespread, though the focus in this study is drawn to rheology of moderately dense systems, $\phi_s = 0.55$. On the industrial side, accurate models for μm-sized powder rheology are vital for the simulation and modeling of Geldart C powders in fluidized bed processes [9–13]. In processes that depend intimately on the resultant flow field

kinematics, such as in powder mixing [14] and materials processing [15], rheological models of dry cohesive powders must predict the correct yield stress behavior in order to achieve success. In extraterrestrial settings, rheology is of importance for understanding the transport of and contamination by Martian and lunar regolith [16] as well as for asteroid mining [17,18]. The discrete element method (DEM) will be used to extract rheological scalings that are relevant to constitutive modeling in these many different contexts.

The most unique phenomenon brought on by cohesion is a transition from fluidlike behavior to solidlike behavior, which directly depends on both shear rate and cohesive strength [1,3,19]. This transition is observed to occur both in the presence [1,3] and absence of friction [19,20]. Several generic characteristic features also accompany this transition, which are observed in different combinations of frictional and frictionless systems, two and three dimensions, and at constant volume or constant pressure. An increase in particle contacts is observed as the shear rate is decreased or cohesion is increased near the transition for frictional systems [3], reminiscent of the transition with volume fraction in noncohesive systems. Shear banding [3–5,8,21] and more elaborate instabilities [20] have also been observed as cohesion is increased in very large systems. However, as cohesion is increased beyond some critical value, shear banding may disappear [3]. An increase in a correlation length scale for correlated nonaffine particle velocities is also observed [22].

Some noteworthy differences from noncohesive systems have also been reported in the study of cohesive granular systems. For frictionless systems below a certain shear rate or strength of cohesion, homogeneous macroscopic systems become thermodynamically unstable [20] and can exhibit negative pressures [5]. Most puzzling is that the transition in frictionless systems is considered energetic in nature, depending only on collisional energy dissipation, van der Waals potential, and shear rates. The rheological behavior of frictional

*Corresponding author: shankar@iastate.edu

systems, on the other hand, has often been collapsed by a dynamic scaling, i.e., using the cohesive force at contact [1,3,22]. Whether both scalings are correct and how the transition between scalings happens for vanishing interparticle friction remain unanswered.

Moreover, a clear microscopic and mechanistic picture of why this transition occurs, and an explanation for the differences between frictional and nonfrictional cases, is lacking. It is known from the standpoint of the kinetic theory of frictionless cohesive spheres that aggregation of particles is sensitive to granular temperature, which scales with the macroscopic shear rate squared [10,19,23,24]. How this aggregation mechanism fully connects to the observed rheological transition remains an unanswered question.

In our DEM studies, we find an important connection for both frictional and frictionless systems between the fluid to solidlike transition and the ratio of the cohesion energy to the granular temperature and explore this connection in detail. For frictionless systems the scaling is robust for all coefficients of restitution. Microstructural measures are introduced, such as a cluster length scale, which clearly shows that the mechanism behind the rheological transition in frictionless systems is percolation of the domain by particle contact networks. Additionally, nontrivial trends in the shear stress ratio with varying friction are explored and connected to contact anisotropy.

The results obtained herein hint at some difficulties in the constitutive modeling of cohesive granular flows. It is now understood that in ordinary granular flows, nonlocal rheological behavior is tied to the granular temperature both through interaction with boundaries [25,26] and increase in local nonaffine velocity correlations that determine collisional energy dissipation [27,28]. The temperature in these cases is not slaved to the local shear rate and pressure, as is the case in the so-called $\mu(I)$ rheology [29]. We expect that the sensitive dependence of the rheology on granular temperature will also mean that additional transport models for variables, namely temperature, will need to be considered in addition to flow kinematics. Lastly, the emergence of new diverging cluster length scales must also be accounted for in any proposed rheological model.

II. METHODS

In this paper we aim to examine the physical basis for the transition in rheological scaling in simple shear, from inertial to quasistatic scaling, for moderately dense assemblies of cohesive granules. To accomplish this analysis we have performed DEM simulations of simple shear using the molecular dynamics code LAMMPS [30]. Particles in this methodology interact not only due to the ordinary elastic and dissipative models that are active when particles are in contact, but also due to an attractive potential well, which extends beyond contact [19,23]. A generic form of the normal component of the combined contact force law and cohesive force law are given by

$$
\mathbf{F}_n^{(ij)} = \begin{cases} (R_{\text{eff}}|\delta|)^p\big(-b_n\mathbf{v}_n^{(ij)} - k_n\delta\hat{\mathbf{n}}^{(ij)}\big) + \mathbf{F}_{c,vdW} & : \delta \leqslant 0 \\ \dfrac{-AR_{\text{eff}}}{6(\delta+d_0)^2}\hat{\mathbf{n}}^{(ij)} & : \delta > 0 \end{cases}
$$

$$(1)$$

where b_n and k_n are the normal damping and spring constants of the force law. These forces depend on $\mathbf{n}^{(ij)}$, the normal separation vector from particle i to particle j, the surface separation or overlap $\delta = |\mathbf{n}^{(ij)}| - (R^{(i)} + R^{(j)})$, and pair normal velocity $\mathbf{v}_n^{(ij)}$. Lastly, a caret indicates a unit vector. The van der Waals force is the source of cohesion in this model and is determined by the Hamaker constant A, effective radius at contact $R_{\text{eff}} = R^{(i)}R^{(j)}/(R^{(i)} + R^{(j)})$, which may differ from the radius of the particle, and the interatomic separation distance d_0, typically taken to be anywhere from 0.167–0.4 nm [1,12,19,31]. In this model, the van der Waals force saturates at contact and hence the cohesive force between a pair of particles in contact is given by $\mathbf{F}_{c,vdW} = -\hat{\mathbf{n}}^{(ij)}AR_{\text{eff}}/(6d_0^2)$. This model is consistent with approaches for nearly rigid particles where the Tabor parameter is sufficiently small $\mu_T < 0.1$ [32] and the radius of contact is sufficiently large $R_{\text{eff}} \gg d_0$ [31]. Finally, the exponent p is used to select between contact force models such as the linear spring dash pot [33], $p = 0$, and the Kuwabara-Kono model $p = 1/2$ [34,35].

The tangential forces are governed by similar models given by

$$
\mathbf{F}_t^{(ij)} = \begin{cases} (R_{\text{eff}}|\delta|)^p\big(-b_t\mathbf{v}_t - k_t\mathbf{u}_t^{(ij)}\big) & : \delta < 0, |F_t| \leqslant |\mu_f F_n| \\ -\mu_f|F_n|\hat{\mathbf{u}}_t^{(ij)} & : \delta < 0, |F_t| \geqslant |\mu_f F_n|, \\ 0 & : \delta > 0 \end{cases}
$$

$$(2)$$

where a subscript t is used to indicate the tangential counterpart of the normal definitions. Additionally, $\mathbf{u}_t$ is the elastic surface displacement. The tangential force saturates as well, when a yield criterion is met, see Eq. (2). Thereafter, a Coulomb friction law is used, where μ_f is the coefficient of friction. The tangential spring stiffness is taken to be $k_t = 2k_n/7$ [36], when friction is present. The tangential damping is set to zero and not considered in our treatment.

The parameter space of interest for these systems is best discussed in nondimensional terms. The normal force law given in Eq. (1) produces four independent nondimensional groups [19]. The groups for the linear spring dash-pot variant that we will choose to use are the ratio of the attractive potential at contact to the kinetic energy in the relative normal direction $\text{Ha}_p = 2AR_{\text{eff}}/(6m_{\text{eff}}v_{\text{ref}}^2 d_0)$, the modified Bond number [1] $\text{Bo}^\star = AR_{\text{eff}}/(6d_0^2 kD)$, the coefficient of restitution ε, and the scaled particle stiffness $k^\star = k/(\rho Dv_{\text{ref}}^2)$. Note that the coefficient of restitution is given by $\varepsilon = \exp(-\pi/\sqrt{(4k_n m_{\text{eff}})/b^2 - 1})$. The tangential force law also produces the important nondimensional group already introduced μ_f. Here the effective mass is given by $m_{\text{eff}} = m^{(i)}m^{(j)}/(m^{(i)} + m^{(j)})$ and ρ is the particle density. Since we are considering simple shear flows of granular particles the reference velocity v_{ref} can be chosen to be one of two macroscopic velocity scales: the granular temperature $v_{\text{ref}} = \sqrt{T_g} = \sqrt{\langle v_k'^{(i)}v_k'^{(i)}\rangle/3}$ or the velocity scale defined by the shear rate $v_{\text{ref}} = \dot{\gamma}D$. Both of these reference velocity scales will be used to define a macroscopic Ha_α parameter, where α is a placeholder for the shear rate $\dot{\gamma}$ or temperature T. Additional macroscopic nondimensional groups are then $T/(\dot{\gamma}D)^2$, the solid volume fraction ϕ, inertial scaling of pressure related to the so-called inertial number [29,37] by $P/(\rho(\dot{\gamma}D)^2) = I^{(-2)}$, and of course any number
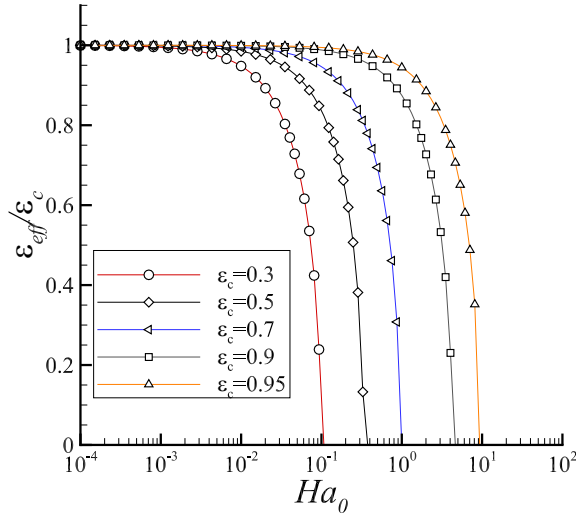
FIG. 1. The behavior of ε_{eff} the effective coefficient of restitution is plotted for several values of ε. Systems with higher intrinsic inelasticity require weaker potential wells to lead to sticking.

FIG. 2. The appearance of clusters in a snapshot where $\text{Ha}_{\dot{\gamma}} = 0.72$, $\text{Bo}^{\star} = 4.2 \times 10^{-10}$, and $D/d_0 = 10^4$.

of ratios between combinations of entries in the stress tensor, e.g., shear stress ratio $\mu = \sigma_{xy}/P$.

Aarons and Sundaresan [1] and Gu *et al.* [3] investigated a transition in stress behavior in sheared cohesive assemblies that occurs at volume fractions below the jamming transition for noncohesive particles. In this paper we are interested in the physical underpinnings of the transition of assemblies of cohesive particles with and without friction. Toward this end we have chosen to simulate a solid volume fraction of $\phi = 0.55$, while varying other relevant parameters such as ε, $\text{Ha}_{\dot{\gamma}}$, $\text{Bo}^{\star}$, and μ_f.

Previous studies on head-on collisions of cohesive particles have revealed that for particles that are sufficiently hard, e.g., with stiffnesses satisfying $\text{Bo}^{\star} < 10^{-5}$ for $\varepsilon = 0.9$ and $D/d_0 = 10^4$, the restitution behavior is purely a function of the parameter Ha_p and ε [12,19]. Here the reference velocity is the initial relative velocity between a pair of particles separated beyond the strong cohesive part of the well, at least $10d_0$. The equation for the effective coefficient of restitution ε_{eff} is then given by

$$\varepsilon_{\text{eff}} = \begin{cases} (\varepsilon^2 - (1-\varepsilon^2)\text{Ha}_p)^{1/2} & : v_{\text{ref}} \in (-\infty, v_{\text{crit}}) \\ 0 & : v_{\text{ref}} \in [v_{\text{crit}}, 0] \end{cases}, \quad (3)$$

where the critical initial velocity is $v_{\text{crit}} = -\sqrt{2AR_{\text{eff}}(1-\varepsilon^2)/(6d_0 m_{\text{eff}}\varepsilon^2)}$ and the corresponding $\text{Ha}_{\text{crit}} = \varepsilon^2/(1-\varepsilon^2)$. The plot of this restitution behavior can be found in Fig. 1. This equation first appeared in a treatment by Dahneke [38], who was investigating the restitution behavior of μm-sized latex spheres impacting a wall. Figure 1 shows two important behaviors: (i) near the critical velocity an increase in cohesion or decrease in velocity increases dissipation in a particle collision; (ii) particles with lower restitution coefficient stick together more easily. We expect this change in restitution and sticking behavior brought on by cohesion to play a significant role in the formation of structure during the regime transitions observed in simple shear, especially for frictionless particles.
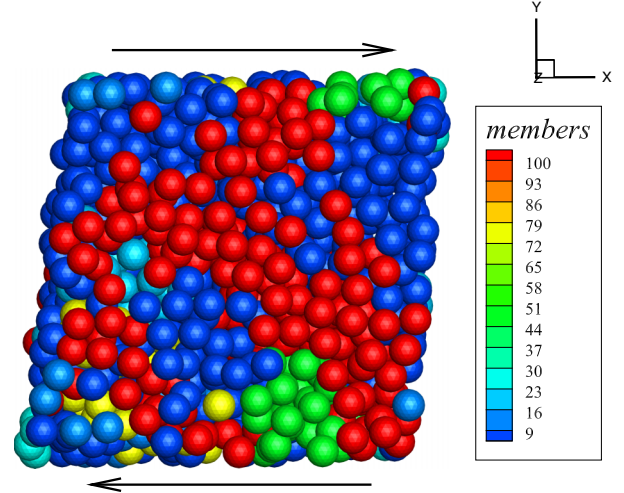
DEM simulations of simple shear are carried out using a triclinic deforming domain, equivalent to the Lees-Edwards boundary conditions [39] at constant volume. In this setup energy is added to the kinetic energy of the domain through the usual mechanism of viscous heating $\dot{E}_{\text{kin}} = \sigma_{xy}\dot{\gamma}$. This heating generates fluctuations in the particle velocities, which are eventually dissipated by collisional and frictional dissipation mechanisms. We expect that for frictionless systems if the characteristic velocity set by the granular temperature is much greater than the critical velocity, cohesion will play little to no role.

As the temperature approaches its value corresponding to the critical velocity, the formation of larger clusters is to be expected (see Fig. 2). Eventually, we expect that clusters must become large enough to span the computational domain. The percolation of clusters changes the mechanism of momentum transfer from collisional to yielding. The shear stress should then become quasistatic in nature, i.e., $\sigma_{xy} \sim \dot{\gamma}^0$, consistent with dense flows near the jamming transition for noncohesive particles [3,40]. How exactly this transition occurs and how it affects the formation and breakup of aggregate structure remains a mystery.

In the following section we first explore the behavior of macroscopic quantities, such as shear stress, temperature, and shear stress ratio, near the inertial to quasistatic transition. The relevant nondimensional parameters used in the following studies is given in Table I. We then look at microscopic and cluster measures as a means to explain the emergence of different scaling behaviors in the macroscopic variables. Finally, we look at the contact anisotropy to explain differences in shear stress ratios with and without friction.

III. RESULTS

Section III is divided into four subsections. The first section explores the behavior of macroscopic observables, such as shear stress, shear stress ratio, and granular temperature, at shear rates both above and below the transition. Differences that arise between frictionless and frictional systems are also

TABLE I. Parameters used in simple shear simulations of cohesive granules.

Parameter	Values
ϕ	0.55
ε	$0.7; 0.8; 0.9; 0.95; 0.99$
$\mathrm{Ha}_{\dot{\gamma}}$	7.2×10^{-5}–7.2×10^{2}
$\mathrm{Bo}^{\star}$	4.2×10^{-14}–4.2×10^{-5}
$k^{\star}$	2×10^{8}–10^{13}
D/d_0	10^{4}–10^{5}
μ_f	$0; 10^{-5}; 10^{-4}; 10^{-3}; 10^{-2}; 10^{-1}; 5 \times 10^{-1};$

discussed. The second section focuses on microscopic quantities such as the local average potential and average cluster length scales. Scaling of all these quantities is also discussed. In the third section, a connection between contact anisotropy and shear stress ratio behavior is discussed. Finally, challenges in constitutive modeling are discussed.

A. Energetic collapse of stress

The shear studies presented here are all performed at a volume fraction, $\phi_s = 0.55$, below the jamming transition as defined by Chialvo *et al.* [40]. For noncohesive particles, momentum transport still occurs primarily due to collisional transport, and Bagnold [41] or inertial scaling of the stress is observed. Previous studies in the moderately dense regime, i.e., $\phi_s = 0.45 - 0.6$ at constant volume for cohesive frictional particles have shown an additional transition in the rheology due to the sticking and clumping of particles [1,3,42]. This transition was shown to depend on the cohesive force scaled by inertial terms, i.e., the product $\mathrm{Bo}^{\star}k^{\star}$. Recent simulations [20] and theory [43] for sheared systems of cohesive frictionless particles, modeled through a Lennard-Jones potential, also reveal a transition in the rheological behavior. When cohesion is below some threshold value, dispersed particle assemblies were obtained [20]. However, when the shear rate became small enough or cohesion large enough, particle assemblies became thermodynamically unstable [43] and formed various patterns. The location of the thermodynamic instability was shown to scale with both the inelasticity $\alpha = 1 - \varepsilon^2$ and a term s analogous to $\mathrm{Ha}_{\dot{\gamma}}^{-1}$, in agreement with Eq. (3). We now explore how this transition occurs using our force model in Eq. (1), and how the introduction and variation of friction changes this transition.

Figure 3(a) displays the results of shear simulations for frictionless particles at different values of inelasticity, $\mathrm{Ha}_{\dot{\gamma}}$, $\mathrm{Bo}^{\star}$, and D/d_0, i.e., varying the Hamaker constant, shear rate, and particle size relative to the interatomic distance. There is indeed a transition in the shear stress from inertial to quasistatic scaling for all cases. The location of the transition appears to depend only on the inelasticity of the equivalent noncohesive model, with the more elastic systems requiring lower shear rates to become fluidized and achieve inertial scaling, as compared to less elastic granules. This is consistent with expectations from Eq. (3) for ϵ_{eff} which determines the critical velocity. We note that the critical value of $\mathrm{Ha}_{\dot{\gamma}}$ is not identical to $\mathrm{Ha}_{\mathrm{crit}}$. For example, for $\varepsilon = 0.99$ the critical value of $\mathrm{Ha}_{\mathrm{crit}} \approx 50$ while $\mathrm{Ha}_{\dot{\gamma},\mathrm{crit}} \approx 10$. Further, the scaled shear
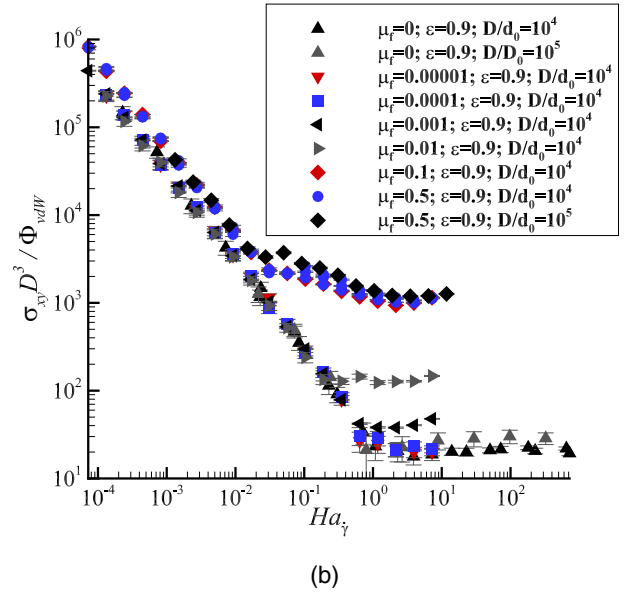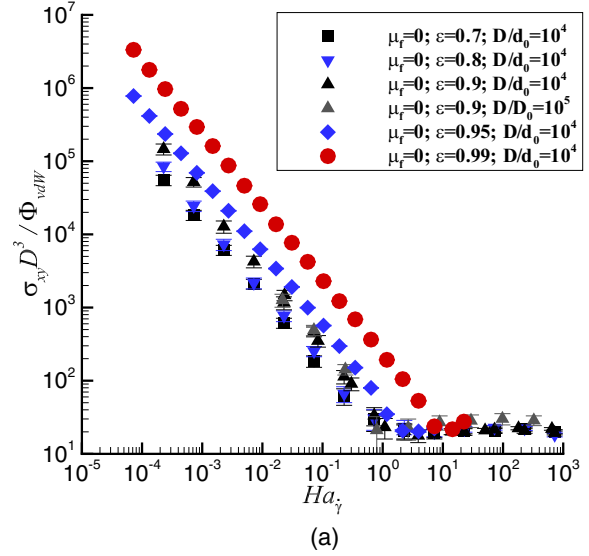

FIG. 3. (a) The collapse of shear stress for frictionless spheres with squared inverse shear rate, i.e., $\mathrm{Ha}_{\dot{\gamma}} \sim \dot{\gamma}^{-2}$. The collapse is also energetic depending only on the coefficient of restitution. (b) The same collapse is given for spheres with varying strengths of friction and same coefficient of restitution. The collapse remains energetic.

stress in the quasistatic regime is practically identical for all cases. The most important takeaway from this plot is that the two values of D/d_0, as used in the $\varepsilon = 0.9$ cases, yield the same qualitative behavior (location of the transition) and quantitative behavior (magnitude of the shear stress). In the model used, two different values of D/d_0 allow us to determine whether a scaling is truly dynamic or energetic. A dynamic scaling [1,3] is scaled by a characteristic cohesive force proportional here to d_0^2, while an energetic scaling [19,23,43] utilizes a cohesive potential Φ_{vdW} at contact, proportional to d_0. When two different values of D/d_0 are compared, a collapse of the stress can be only energetic or dynamic, but not both. The collapse here is clearly energetic. We may infer that it

is the granular temperature, i.e., velocity fluctuations, that is important in determining transition behavior here, rather than a coherent forcing imposing the shear profile in the mean velocity.

Cases with varying strengths of friction from quite small $\mu_f = 10^{-5}$ to rather large $\mu_f = 0.5$ are also shown in Fig. 3(b), all for a coefficient of restitution of $\varepsilon = 0.9$. A similar behavior is found here in regard to the effect of friction. The critical value of $\mathrm{Ha}_{\dot{\gamma}}$ decreases with increasing friction, meaning that as friction is increased a higher shear rate is necessary to achieve fluidization. We notice that for small enough friction, e.g., $\mu_f \leqslant 10^{-4}$, there is practically no difference between stress scaling in frictionless and frictional systems. The two most important observations are (i) the location of the transition in stress scaling remains energetic in the presence of friction for $\mu_f = 0.5$ and differing D/d_0 and (ii) the scaled stress in all regimes scales energetically. The origin of this transition with and without friction appears to be brought about primarily by energy loss in collisions leading to sticking, which is only affected by the coefficients of restitution and friction.

Finally, we note that the frictional cases saw many instabilities emerge in the quasistatic regime, e.g., shear banding [3,43], so-called flying ice cubes, and crystallization. Because those instabilities are of little interest in the present study, data points exhibiting the instabilities have been removed from the data presented here. Nonetheless, all data in the inertial regime were stable, and the critical value of $\mathrm{Ha}_{\dot{\gamma}}$ remained solely determined by ε and μ_f.

Now we explore the transition in more detail, namely a collapse using the granular temperature rather than shear rate as a characteristic velocity scale. Figure 4 displays the shear stress and temperature scaling for frictionless systems as a function of Ha_T. The location of the transition in stress for frictionless systems occurs at a unique Ha_T for all values of ε, with $\mathrm{Ha}_{T,\mathrm{crit}} = 1$. Minor differences in stress magnitudes occur in the inertial regime for different ε due to differences in dashpot strength. Lastly, the frictional cases do not all transition at
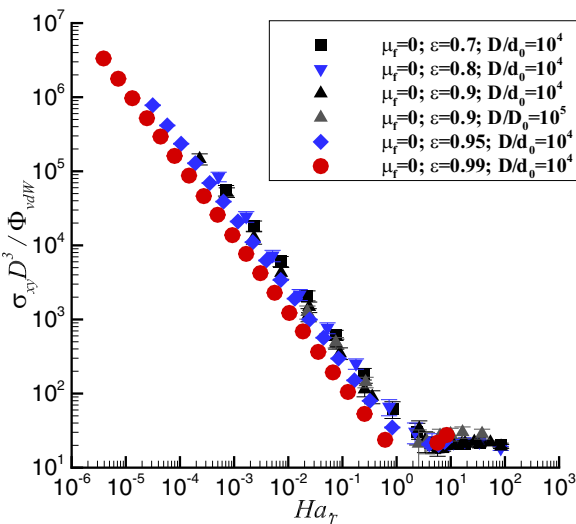
$\mathrm{Ha}_T = 1$. A more detailed characterization of the behavior of the temperature, and an explanation as to why collapse occurs at $\mathrm{Ha}_T = 1$ can be found in Appendix A.

The often used $\mu(I)$ rheology [29] focuses on the behavior of the shear stress ratio $\mu = \sigma_{xy}/p$ or apparent friction coefficient of the granular assembly. Cohesion is observed to increase the apparent friction, allowing for different values of μ to be observed at the same volume fraction, as was previously observed [3,21,22]. Here we are interested in how the pressure might scale differently from the shear stress. Figures 5(a) and 5(b) display the apparent friction for frictionless and frictional systems, respectively. In the absence of friction, we see that all cases more or less scale the same in both the inertial and quasistatic regimes. The cases in the quasistatic regime show much larger values for the apparent
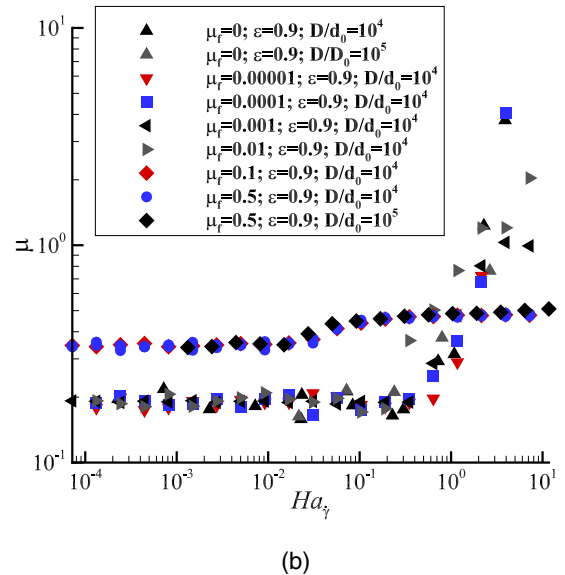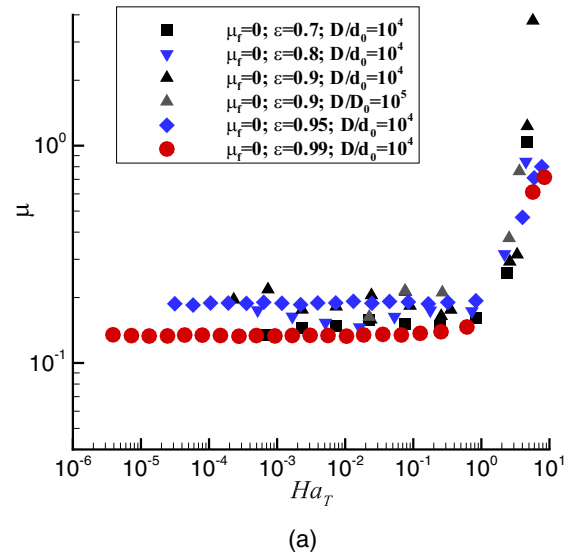

(a)

(b)

FIG. 5. (a) The behavior of the apparent friction is compared among frictionless assemblies with differing coefficients of restitution. (b) The apparent friction for cases with varying friction and $\varepsilon = 0.9$.

FIG. 4. An improved collapse of shear stress, with the characteristic velocity scale based on temperature rather than shear rate.

friction as compared to that in the inertial regime, i.e., low Ha_T. Small differences are also observed in μ due to the coefficient of restitution as well. Most interestingly here we observe values of μ that exceed unity, consistent with previous studies in the moderately dense regime [19,22]. The reason for this is that the frictionless systems are observed to be metastable for $Ha_T > 10$, with negative pressures developing. Negative pressures have also been observed in frictionless studies of two-dimensional (2D) attractive systems [5]. As the pressure approaches zero, the apparent friction may become large. In a large enough domain these systems should phase separate into dense and dilute phases, consistent with prior studies [4,20]. This phase separation is beyond the scope of this work.

In frictional cases, it is seen that if the friction is small enough, e.g., $\mu_f < 0.1$, similar behavior in the apparent friction is observed. With higher particle friction, the apparent friction begins at $\mu \approx 0.35$ and saturates at a value of $\mu \approx 0.5$ in the quasistatic regime. For very low friction, $\mu_f < 10^{-4}$, some values of μ are still greater than unity. Here again, negative pressures are observed. The microstructural origin for the differing behaviors in μ for large and infinitesimal friction will be explored in Sec. IIIC.

B. A signature of transition in rheology

The physical underpinnings of the inertial to quasistatic regime transition in granular flows are now explored. A strong correlation has been observed between particle sticking brought on by enhanced collisional dissipation due to cohesion, and the location of the regime transition. This leads us to believe that it is the formation of clusters that is ultimately responsible for the regime transition. An average length scale $\langle \xi_i \rangle$ is now introduced in order to observe this transition

$$\xi_i^l = \max \frac{n_i^{(jk)}}{2} \quad \forall \quad j,k \in \mathcal{C}^l$$

$$\langle \xi_i \rangle = \frac{1}{N_p} \sum_{l=1}^{N_c} N_{p,l} \xi_i^l. \tag{4}$$

Here $\boldsymbol{n}^{(j,k)}$ is the normal separation vector between centers of particles j and k, $\mathcal{C}^l$ is the set of particle indexes in cluster l, and N_c and $N_{p,l}$ denote the number of clusters and number of particles in a cluster, respectively. Note that we consider particles to be clustered with one another if they are in physical contact, i.e., $\delta \leqslant 0$. It has also been shown that the length scale is not significantly affected by the stiffness of particles once clusters begin to develop and if particles are hard enough [19], i.e., $Bo^\star < 10^{-5}$. The clustered contacts endure on much longer time scales than collisional time scales. The coordinate system that ξ_i is based on is aligned with the original box dimensions. Note that this quantity is not a true vector because it does not transform as one. This length scale represents the farthest that a disturbance to a particle can travel on average through an aggregate, or half the length of an aggregate in the ith direction. If this length scale reaches half the size of the box then the box is percolated in the ith direction, and a disturbance can reach any location in that direction. The direction of interest here is the shear direction, since shear is maintained through momentum being imparted on particles crossing the boundary
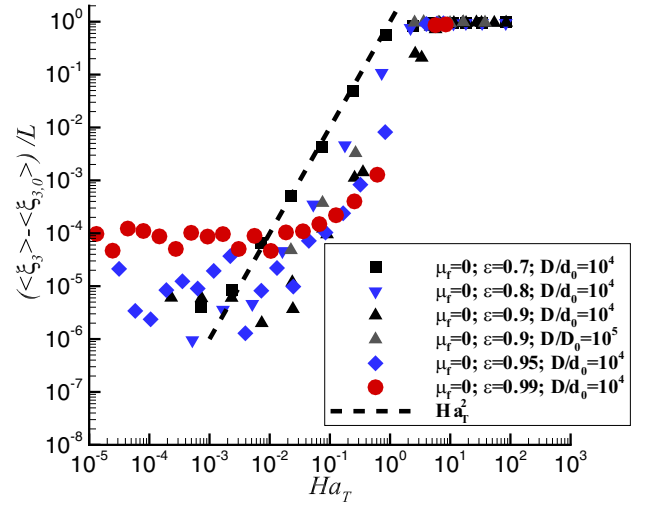
(a)
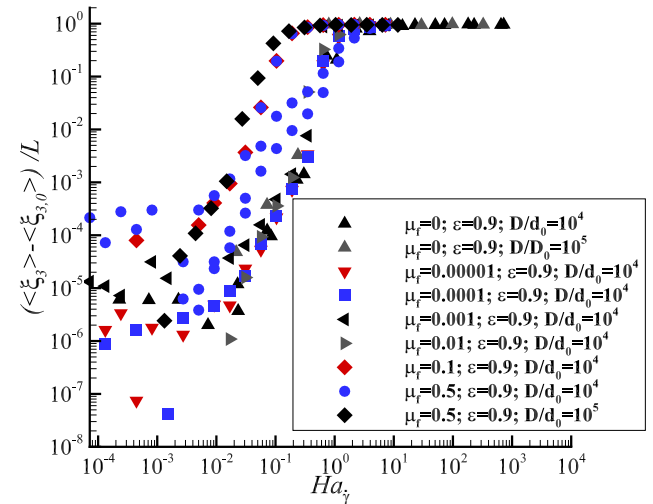
(b)

FIG. 6. (a) The scaling of the average cluster length-scale in the shear direction is given for frictionless spheres, which scales as Ha_T^2. Percolation is observed for $Ha_T > 1$. (b) The cluster length scale is given for varying coefficient of friction. Percolation does not correlate with the transition for all cases.

in this direction. There are other measures of the length scale of particle clusters that do not depend on the coordinate system, such as the radius of gyration tensor. However, this measure is also sensitive to the packing of particles (i.e., dimension of the aggregates). While they behave similarly to the length scale introduced here, they do not clearly demonstrate the physics of the diverging length scale. Finally, we note that monomers do not contribute to the length scale ξ_i^l, but they do contribute to the average length scale $\langle \xi_i \rangle$ due to the normalization.

We now look to the average cluster length scales in Figs. 6(a) and 6(b). The reported length scale $\langle \xi_3^\star \rangle = 2(\langle \xi_3 \rangle - \langle \xi_{3,0} \rangle)/L$ subtracts off the value observed for an equivalent case without cohesion and is normalized by the height of the cubic domain. The value of $\langle \xi_3^\star \rangle$ at low Ha_T and $Ha_{\dot\gamma}$ should be zero and the

scatter is merely due to statistical variability. Impressively, if we compare the average length scale for frictionless particles in Fig. 6(a), we find that the length scale grows exactly as Ha_T^2, which is predicted from scaling arguments for population balances in Appendix B. For the case of $\varepsilon = 0.7$ this occurs not only for $Ha_T \ll 1$ but also until the length scale saturates at the size of the box. Percolation of the contact network is the result of the average length scale reaching the size of the box, and coincides well with the inertial to quasistatic regime transition at $Ha_T = 1$. Animations to demonstrate the percolation for a few cases with varying $Ha_{\dot\gamma}$ are provided in the Supplemental Material [44]. There we observe that when $Ha_{\dot\gamma}$ is small, few aggregates are observed and are mostly dimers. As $Ha_{\dot\gamma}$ is increased, large fluctuations in aggregate size are observed, which is consistent with phase transition phenomenology. At the largest values of $Ha_{\dot\gamma}$ only a single aggregate is observed with small transient aggregates occasionally breaking off and being reabsorbed. The variance in the cluster size distribution (not shown for brevity) peaks during the stress transition.

For frictional cases, we observe that percolation does not always coincide with the rheological transition. For cases where $\mu_f = 0.5$ and $D/d_0 = 10^4$ with the same values of $Ha_{\dot\gamma}$ but different shear rates, differing values of $\langle \xi_3^\star \rangle$ are observed. All three contain an inflection point at the same $Ha_{\dot\gamma}$, but percolation, as defined by this quantity, is observed at different points. Note that all cases yield shear stresses that are practically identical. The differences in length scales are likely due to differences in the stiffness and thus contact duration.

For frictional cases, a better structural indicator of the stress transition is a jump in the average local cohesive potential, $\langle \Phi_{\mathrm{loc}} \rangle / \langle \Phi_{vdw} \rangle$. This is the average total local potential of a particle and all of its neighbors normalized by the potential between two particles in contact, which has been used previously to characterize aggregates in shear flow of nanoscale particles [45]. Due to the extremely short-ranged nature of these potentials, this is a good surrogate for the coordination number in these stiff systems. Figures 7(a) and 7(b) give the scaled potential for both frictionless and frictional cases. For strongly frictional cases $\mu_f \geqslant 0.1$, the location of the transition coincides with a marked rise in $\langle \Phi_{\mathrm{loc}} \rangle / \langle \Phi_{vdw} \rangle$ to $\langle \Phi_{\mathrm{loc}} \rangle / \langle \Phi_{vdw} \rangle \approx 2$ in agreement with Gu *et al.* [3]. For cases with smaller friction, the jump is more extreme, to $\langle \Phi_{\mathrm{loc}} \rangle / \langle \Phi_{vdw} \rangle \approx 4$. Increasing $Ha_{\dot\gamma}$ at larger μ_f generally leads to smaller $\langle \Phi_{\mathrm{loc}} \rangle / \langle \Phi_{vdw} \rangle$. This seems to be in agreement with the notion that chains of particles are more stable against buckling as friction is increased, so that fewer redundant contacts are needed to stabilize the local particle arrangement. Finally, we note that all cases have $\langle \Phi_{\mathrm{loc}} \rangle / \langle \Phi_{vdw} \rangle < 6$, the coordination number for isostatic jamming of frictionless spheres [46].

C. Contact anisotropy

Lastly, we examine the microscopic ordering that gives rise to the observation that including friction leads to an increase in shear stress in the quasistatic regime but a decrease in shear stress ratio. Evidence has already been shown in Fig. 7(b) that lower friction leads to more compact aggregates. The virial components of the stress tensor $\sigma_{ij} = \Sigma_{k \neq l} n_i^{(kl)} F_j^{(kl)} / V$ show us that the alignment between forces and lines of
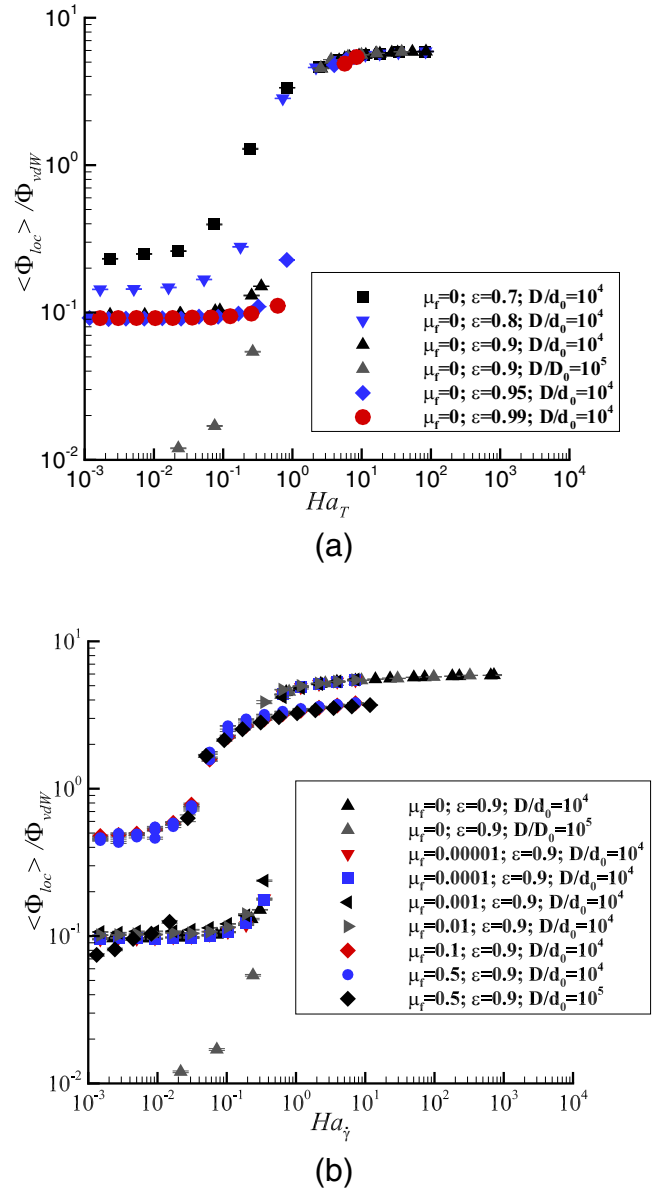

FIG. 7. (a) The scaled average local cohesive potential is given for frictionless cases. A jump in the potential is shown for all cases at $Ha_T = 1$. (b) The scaled average local cohesive potential for frictional cases shows a marked increase that correlates well with the stress transition.

center for particles in contact is important in determining how the shear stress and shear stress ratio should scale. Here V is the volume of the simulation domain. To that end we extract the radial distribution function at contact in spherical coordinates $g(r = D, \theta, \phi)$ and decompose this function into tesseral spherical harmonics. Here θ is the polar angle at which particles are separated in relation to the axis of shear in the counterclockwise direction, while $\phi = 0$ is aligned with the negative streaming direction. Spherical harmonics are an extension of Fourier series with spherical periodicity rather than circular periodicity. In this sense, spherical harmonics are a natural extension to the Fourier decomposition used to represent contact anisotropy in two dimensions [21].

The first spherical harmonic mode is isotropic, and contains information about the isotropic radial distribution function at contact, i.e., $g_c = g(r = D)$. The next spherical harmonic mode that we consider has both the reflective symmetry required in $g(r = D, \theta, \phi)$ and also aligns with the eigenvectors (compression and extension) of the imposed shear flow, while ignoring additional structure in the transverse direction. Lower-order modes were also computed as discussed below but yielded amplitudes close to zero. The decomposition in orthonormalized tesseral spherical harmonics is as follows:

$$g(r = D, \theta', \phi') = u_0^0 Y_0^0 + u_2^1 Y_2^1 + \dots$$
$$= \frac{1}{2\sqrt{\pi}} \left(u_0^0 + \sqrt{15} u_2^1 \cos \phi' \cos \theta' \sin \theta' + \dots \right). \quad (5)$$

The mode coefficients are given by u_l^m, while the mode is given by Y_l^m. The subscript l and the superscript m are indexes for the series terms which go from $(0, \infty)$ and $(0, l)$, respectively. The magnitude of the mode is then found via the orthogonality condition as $\delta_{lj}\delta_{mk} = \int_0^\pi \int_0^{2\pi} Y_l^m Y_j^k \sin \theta' d\phi' d\theta'$. The new coordinates $\{\phi', \theta'\}$ are the result of performing a rotation on the coordinate system $\{\phi, \theta\}$ by $-\theta_{\text{shift}}$ about the transverse axis. The angle $-\theta_{\text{shift}}$ is chosen such that the magnitude of the first shear anisotropic mode is maximized. This is consistent with a phase shift in Fourier analysis of two-dimensional flows [21]. For reference, the anisotropic mode of interest is shown in Fig. 8 for $\theta_{\text{shift}} = 0$, where it is clear that a peak occurs in the direction of maximal compression and a valley in the direction of maximal expansion. In order to reduce the error in integration in the orthogonality condition due to nonuniform bin areas, the sphere is binned in recursively triangulated bins from an initial octahedron with vertices aligned in the $\{x, y, z\}$ directions, rather than evenly distributed bins in ϕ' and θ'. This method eliminates any sampling bias due to unequal areas,
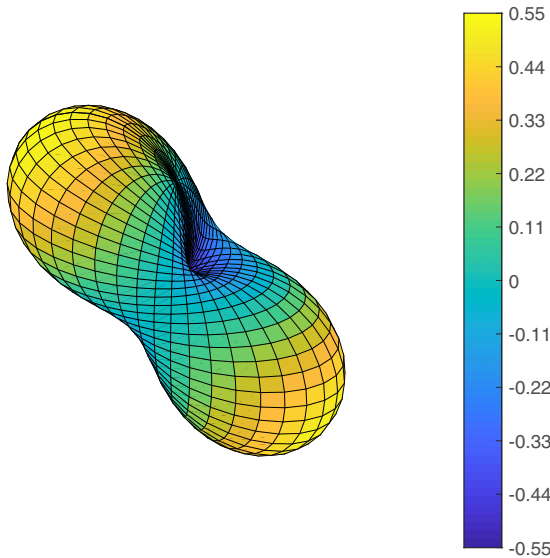

FIG. 8. A depiction of the spherical harmonic mode u_2^1. The sphere has been stretched according to the magnitude u_2^1 at that location. A peak occurs at $(\phi = 0, \theta = pi/4)$ and a valley occurs at $(\phi = 0, \theta = 3pi/4)$.
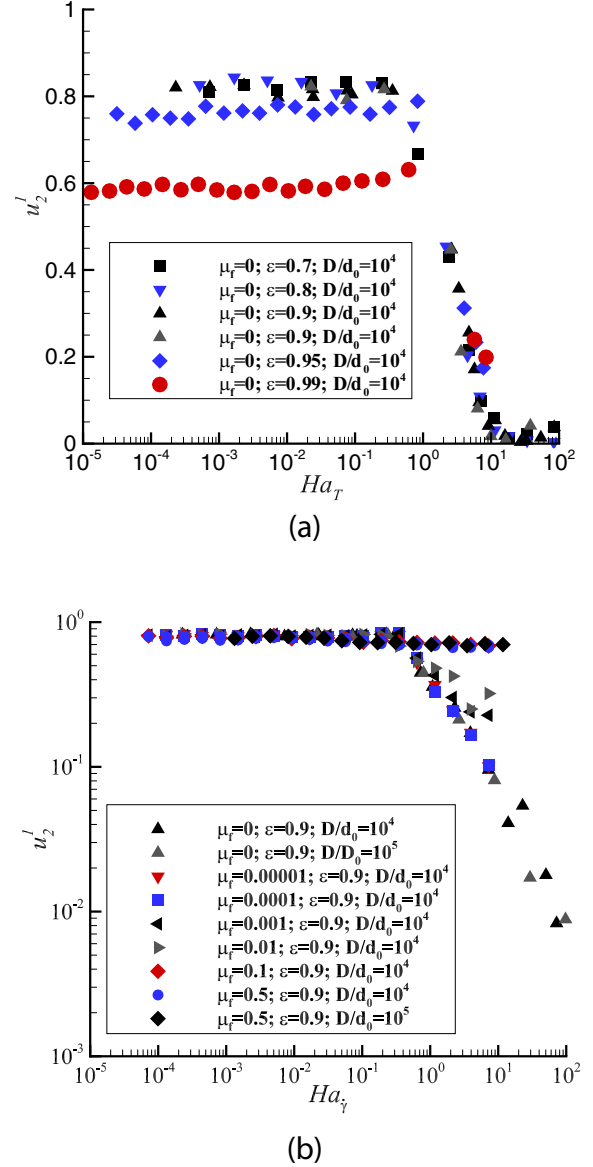

(a)

(b)

FIG. 9. (a) The first anisotropic mode for the frictionless cases show a clearly the effects of temperature, shear rate, and cohesion on the contact anisotropy as represented by u_2^1. (b) The frictional cases show that friction tends to enhance anisotropy in the presence of cohesion.

proportional to $\sin \theta'$, in the uniform ϕ' and θ' sampling. The inclusion of the phase shift in the polar angle θ_{shift} is intended to capture the principal anisotropic mode in the case that the principle directions of the fabric and shear flow are not aligned, which has been observed in split bottom annular shear cell simulations [8]. However, no significant phase shifting was observed here.

Figures 9(a) and 9(b) display the interplay of shear, temperature, cohesion, and friction on the contact anisotropy through the inertial to quasistatic transition. If we focus on the frictionless systems, we see that for all cases, the contact anisotropy collapses above $Ha_T > 1$. For $Ha_T > 1$ the contact anisotropy quickly plummets until above $Ha_T > 10$, where contacts in the system can be considered to be essentially

isotropic. There contacts do not prefer any direction. The isotropic behavior in the quasistatic regime is likely due to unstable particle arrangements in the compression direction, which quickly buckle and rearrange. At values of $\text{Ha}_T < 1$, there are differences in contact anisotropy u_2^1 due to the coefficient of restitution resulting in different temperatures. Each of these different ε have differing scaled temperatures $T/\dot{\gamma}^2$. An increase in scaled temperature, which serves to randomize local velocities, is responsible for the decrease in contact anisotropy brought on by imposed shear. Overall, in the case of frictionless spheres the competition in contact anisotropy appears to be between shear, which enhances anisotropy, and cohesion and temperature, which decrease contact anisotropy.

For frictional cases, we see that friction tends to increase the contact anisotropy in the quasistatic regime [cf. Fig. 9(b)]. Note that these cases are on a log-log plot. For cases where $\mu_f < 0.1$, friction increases the contact anisotropy from what is observed in frictionless cases, though not substantially. For $\mu_f \geqslant 0.1$, we see that although the contact anisotropy is reduced in the quasistatic regime compared to the inertial, consistent with Berger *et al.* [21], the contact anisotropy remains in the same order of magnitude. We attribute the enhancing effect of friction on the contact anisotropy to the increased stability to buckling and rearrangement due to compression. A reduction in the number of sliding contacts was previously observed in two-dimensional studies with cohesion and friction [22].

The origins of the phenomenology observed in the stress and pressure become more obvious when accounting for contact anisotropy. For example, the pressure for frictionless cases with $\text{Ha}_T > 10$ is negative. The contacts in those cases are isotropic. This means that there will be a larger population of particles aligned in the extension direction of the flow, leading to large cohesive tension forces. These forces eventually become larger in magnitude on average than the compressive forces in the spring-damper components. This reduction in pressure due to isotropization of contacts is also responsible for the greater-than-unity shear stress ratios for cases of $\text{Ha}_T \approx 10$, and the metastability for $\text{Ha}_T > 10$.

For frictional cases, the contact anisotropy is less affected by cohesion in the quasistatic regime. There contacts remain anisotropic, and are primarily aligned in the compression direction. This in turn leads to larger pressures, as can be seen in the definition of the pressure due to contacts via the virial expression $P = \Sigma_{k \neq l} n_i^{(kl)} F_i^{(kl)}/(d_f V)$. There d_f are the degrees of freedom. The only components of forces that contribute to the pressure are those aligned with the lines of center between the contacting particles. Here a greater population of particles aligned in the compression direction implies a larger pressure. By contributing to the contact anisotropy, friction indirectly contributes to the smaller values of scaled stress μ in the quasistatic regime. Undoubtedly, the above reasoning also lends to arguments about anisotropy in normal stresses. Though normal stress differences are of interest, they are beyond the scope of the current study.

D. Implications for constitutive modeling

In this paper so far the effect of shear and particle properties, such as the coefficients of restitution, friction, and strength of cohesion, on rheology in a moderately dense system has been

considered. Although the effect of volume fraction is known to have a substantial effect on the rheology of granular systems, even without considering volume fraction, rich behavior is observed that must be considered in continuum modeling of cohesive granular materials. The rheological transition between quasistatic and inertial scaling was found to be energetic in nature regardless of the strength or presence of friction at moderate volume fractions. Moreover, the response of the shear stress ratio intimately depends on the friction and volume fraction of the material, through its affect on the fabric. It is thus worth considering what general set of variables stress must depend on for future work.

Many state-of-the-art cohesive rheological models that are valid for all volume fractions make corrections to the $\mu(I)$ rheology [3,21,22], which considers the stress to be slaved to the local shear rate. Variables such as temperature and local fabric, which transparently affect the stress through the virial equation, must also be slaved. Moreover, these models have chosen to use a dynamic rather than energetic scaling, which has been shown here to be incorrect at moderate densities. Recent work has also shown that there are a number of reasons, such a rheology may be insufficient for describing granular flows in general.

Several works have found that the temperature dynamics are important in many flow setups using noncohesive granules, and thus cannot be described by an unaltered $\mu(I)$ rheology [25,26,28]. There, temperature may be supplied to the system from interactions with the boundaries and be eventually dissipated elsewhere in the flow at large distances from the boundaries. Moderately dense cohesive systems intimately depend on the granular temperature, and hence, we expect that the temperature dynamics will also be important for cohesive granular systems. Additionally, we expect that the cluster length scale should be intimately connected to the correlation length affecting temperature dissipation due to correlated collisions in the extended kinetic theory [27].

In fact, the study of the inertial-elastic transition in noncohesive flows [27] gives tremendous insight as to how one might begin to model cohesive systems, accounting for nonlocal effects. In noncohesive systems there are at least three regimes, which are determined by the volume fraction: inertial, correlated collisional, and quasistatic. The inertial and quasistatic regimes exhibit stress scalings with the shear rate that are identical to those observed at low and high $\text{Ha}_{\dot{\gamma}}$, respectively. The nice aspect of the extended kinetic theory approach is the direct connection to kinetic theory, which allows one to pose dependencies on temperature in addition to the shear rate, and also includes a direct connection to enduring contacts allowing for the treatment of soft spheres. The former aspect enables the extended kinetic theory to treat inhomogeneous problems, where temperature is not fully determined by the local shear rate. An additional similarity is that in both the noncohesive and cohesive transitions, viscosity would be seen to increase with temperature as in a gas in the inertial regime and decrease with temperature in the quasistatic regime as in a liquid. However, there are a few notable differences introduced by cohesion. A new variable becomes important in determining regime boundaries, Ha_T. This ratio of cohesion energy to fluctuation energy controls the transition from inertial to rate-independent quasistatic at moderate densities, and makes the

regime boundaries explicitly dependent on temperature, which is not the case for noncohesive systems. The effects of enduring contacts on the rheology is also evidently necessary once percolation of the contact network has occurred.

Still, other works have found that during certain flow protocols, such as shear reversal, that the microstructural or fabric evolution must also be accounted for, and require their own evolution equations [47,48]. We too found that the orientation of contacts is vital for the correct prediction of shear stress ratios in cohesive flows. How cohesion and its interaction with friction affects the fabric dynamics at these more moderate volume fractions is of interest. Lastly, how the essential underlying nonlocal aspects of the rheology, i.e., percolation, should be accounted for remains a topic of interest.

IV. CONCLUSIONS

A regime transition in simple shear simulations of cohesive granules from inertial to quasistatic scaling of the stress is studied. This transition occurs at volume fractions much lower than those where jamming occurs in repulsive systems. The effects of both restitution and friction on the transition are studied. For frictionless systems, the transition occurs at a ratio of cohesive potential energy to fluctuating kinetic energy Ha_T of unity, for any coefficient of restitution less than unity. A unique yield stress is also observed for all frictionless systems. Friction, on the other hand, is observed to increase both energy dissipation and yield stress and yields nonunique locations for the transition and yield stress. Nonetheless, the transition in the stress only collapses with an energetic scaling of the stress and shear rate, rather than a force or dynamic scaling. The scaled shear stress behavior for all systems is also discussed.

The microscopic origin of the transition is further investigated. For systems without friction, percolation is solely responsible for the transition in stress, correlating well with the location of the stress transition at $Ha_T = 1$. Frictional systems do not necessarily need to percolate at any time step, but correlate well with a large increase in the local cohesive potential energy. The average cluster length scale is also observed to grow as T^{-2}, near the transition in frictionless systems. The scaling is accounted for by population balance arguments for systems with large granular temperatures.

The microstructural origin of nontrivial variation in shear stress ratio with shear rate and cohesive strength is explored. In the quasistatic regime, friction tends to increase the yield stress but decrease the shear stress ratio over a range of coefficients of friction. Contact anisotropy is responsible for this scaling, where friction may prevent the buckling of contact chains in the direction of maximal compression. Without friction, aggregates are easily compressed and contacts quickly isotropize, leading to more contacts in tension and thereby decreasing the pressure.

Lastly, some of the repercussions of the sensitivity of the stress to fluctuating kinetic energy are discussed in light of recent works in noncohesive systems. It is unlikely that the temperature dynamics can be ignored in constitutive modeling and continuum simulation of cohesive systems. Additionally, differences in behavior between different sources of cohesion such as liquid bridging and electrostatics also remain unclear and merit further study.

APPENDIX A: TEMPERATURE SCALING IN HOMOGENEOUS SHEAR OF COHESIVE GRANULAR PARTICLES

To understand the stress vs temperature scaling in Fig. 4 a little better, we look at the temperature response given in Fig. 10. The trends for the temperature in the quasistatic and inertial regimes here can easily be explained by an energy balance. For small $Ha_{\dot{\gamma}}$, $T/(\dot{\gamma}D)^2$ is constant, meaning that $T \propto (\dot{\gamma}D)^2$, which one finds from simple dimensional analysis. However, for large $Ha_{\dot{\gamma}}$, $T/(\dot{\gamma}D)^2 \propto Ha_{\dot{\gamma}}^{1/2}$, which translates to $T \propto \dot{\gamma}D$. Note also that the transition between these two scalings does not appear to be smooth and monotonic in the chosen units shown.

The energy balance at steady state for these systems can be seen as a competition between energy input from macroscopic deformations and dissipation by the viscous dash-pot interaction. The energy input into the temperature equation is equal to viscous heating, i.e., $\dot{E}_{in} = \sigma_{xy}\dot{\gamma}$, while the dissipation of energy is proportional to the energy dissipated by particles and number of iterations. In the collisional or inertial regime the rate of dissipation of granular temperature $\dot{E}_{diss}$ is proportional to $(1 - \varepsilon^2)T^{3/2}$ [49]. The extra $T^{1/2}$ arises from the collisional frequency, which determines how often particles are in contact within a given time period. The shear stress σ_{xy} is proportional to $(\dot{\gamma}D)^2$, and viscous heating $\dot{E}_{in}$ is then proportional to $(\dot{\gamma}D)^3$. The end result yields the result that $T \propto (\dot{\gamma}D)^2$. The dependence of $T/(\dot{\gamma}D)^2$ on the coefficient of restitution in the inertial regime is also explained by these arguments.

For quasistatic flows, particles are always interacting or in contact and the stress does not depend on the shear rate. In that case, one finds that the dissipation is directly proportional to the temperature $\dot{E}_{diss} \propto bT$. The energy input also becomes
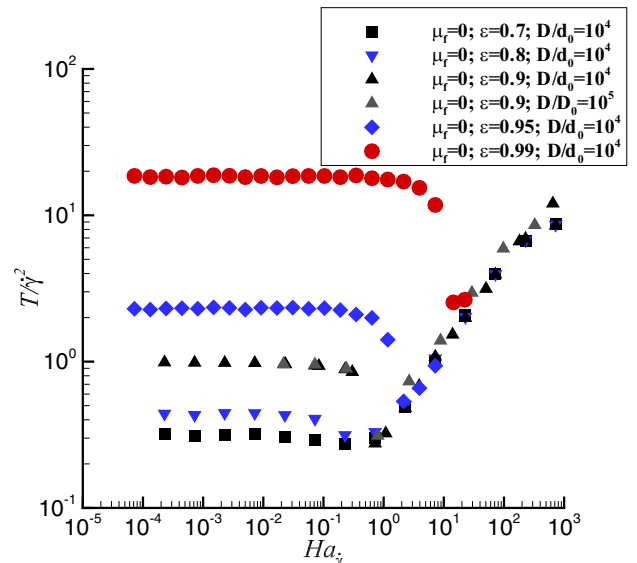

FIG. 10. The scaling of temperature by shear rate for frictionless particles.
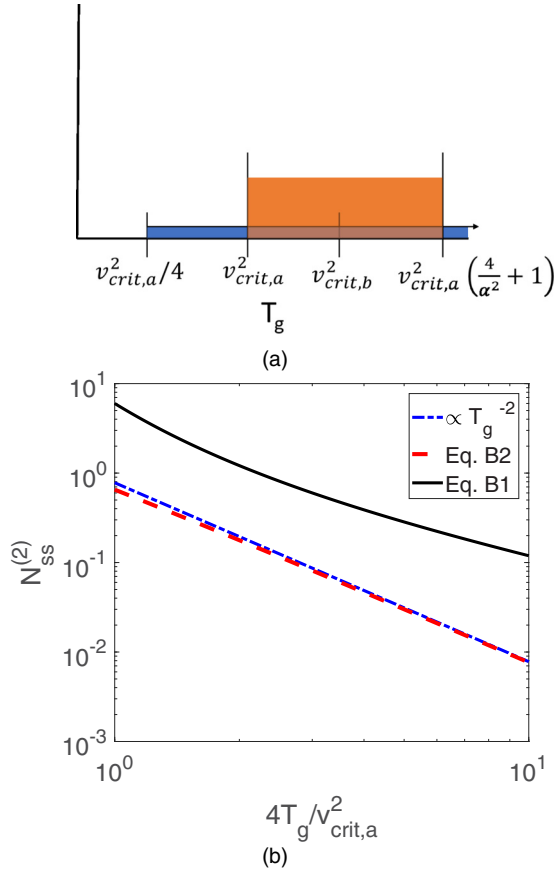
FIG. 11. (a) The temperature regions where the first-order terms in the Taylor series expansions of Eq. (B1) are dominant. The orange indicates the region for the breakup term, while the blue indicates the region for the aggregation term. (b) The scalings of the steady-state dimer population are compared showing that the population scales as $v_{\text{crit,a}}^4/T_g^2$ in the area near the stress transition, using Eqs. (B1), (B2), and a simple T^{-2}.

$\dot{E}_{\text{in}} \propto \dot{\gamma}$, since stress does not depend on the shear rate. Hence, one finds that $T \propto \dot{\gamma}D$ for quasistatic cases. This makes sense from the standpoint of physical intuition as well; in a well-connected assemblage of spheres, fluctuating or nonaffine velocities depend only on rearrangements that are caused by the imposed deformation. Dissipation happens on a much faster time scale (on the order of the collision duration) than particles rearrangements caused by shear. This view is backed up by a unique scaled temperature among differing ε in the quasistatic regime. In a sense, each case with differing ε are kinematically identical if particles are completely clustered.

Finally, in between these two scaling regimes we see a dramatic drop in the scaled temperature, which is likely caused by the sticking of particles and an essential loss of modes that large fluctuating velocities can occupy [23]. This large drop in $T/(\dot{\gamma}D)^2$ is ultimately responsible for the collapse of the stress transition at $\text{Ha}_T = 1$ for frictionless particle systems. We note that frictional cases exhibit the same temperature scaling in the inertial and quasistatic regimes, but as with the scaled shear stress they do not transition at the same Ha_T irrespective of μ_f.

APPENDIX B: SCALING OF THE CLUSTER LENGTH SCALE IN HOMOGENEOUS SHEAR OF MODERATELY DENSE COHESIVE SYSTEMS

Here we explore how the cluster length scale should grow and eventually cause a regime transition in the rheological scaling. The length scale $\langle\xi_i\rangle$ introduced in Sec. III B is normalized by the number of particles in the system. This view essentially considers monomers as clusters of zero length. Incidentally, when only dimers and monomers are present, as is the case for $\text{Ha}_{\dot{\gamma}} \ll \text{Ha}_{\dot{\gamma},\text{crit}}$, the average coordination number $\langle Z \rangle$ will scale exactly the same with $\text{Ha}_{\dot{\gamma}}$ as $\langle\xi_i\rangle$. This is because the length scale for a dimer is essentially constant. In this regime, where $\langle\xi_i\rangle \propto \langle Z \rangle$, we can predict how the cluster length scale might scale with shear rate through the use of population balance equations. The source of dimers due to monomer collisions has been previously derived [23]. A similar integration can be made to estimate the sink of dimers due to collisions that result in breakup. Here we assume that the critical velocity that leads to breakup is slightly larger than the critical velocity under which monomers stick and we assume that this critical velocity is constant. Here $v_{\text{crit,b}} = \alpha v_{\text{crit,a}}$, where $\alpha > 1$. It is also assumed that the sink of dimers must be proportional to the number of dimers present, such that the rate of loss vanishes when dimers are not present. Sources and sinks to larger aggregates are ignored. The resulting rate equation for the number of dimers $N^{(2)}$ is given by

$$\frac{dN^{(2)}}{dt} = C_1\sqrt{T_g}\left[1 - \exp\left(-\frac{v_{\text{crit,a}}^2}{4T_g}\right)\right]$$
$$- C_2 N^{(2)}\sqrt{T_g}\exp\left(-\frac{v_{\text{crit,b}}^2}{4T_g}\right). \quad \text{(B1)}$$

Hereafter we drop the constants C_1 and C_2, since they do not affect the steady-state scaling. To find the leading-order power-law scaling these terms are expanded in Taylor series. Terms in the power series in the temperature range of interest must be less than unity to ensure that higher-order terms are of decreasing importance. Due to the exponential term, neither term can be expanded about $T_g = 0$. The rate of dimer breakup term grows with the temperature, while the rate of monomer aggregation decreases with increasing temperature. We will expand each term around different points, but with overlapping areas where terms up to first order are dominant. The aggregation rate being expanded around $1/T_g = 0$ and the breakup rate around $T_g = v_{\text{crit,a}}^2$. See Fig. 11(a) for a depiction of the areas, where the first-order linear terms are the leading-order terms in the expansion. The steady-state number of dimers is then given to first order as

$$N_{SS}^{(2)} \propto \frac{\dfrac{v_{\text{crit,a}}^2}{4T_g}}{\left(1 - \dfrac{\alpha^2}{4} + \dfrac{\alpha^2 T_g}{4v_{\text{crit,a}}^2}\right)\exp\left(-\dfrac{\alpha^2}{4}\right)}. \quad \text{(B2)}$$

The scaling of the steady-state dimer population is plot in Fig. 11(b). There the raw scaling using Eq. (B1), expansion to first order in Eq. (B2), and the power-law $v_{\text{crit,a}}^4/T_g^2$ term, without the additive constants in the denominator, are compared for

the case of $\alpha = 1.5$ [50]. We see that the slope is quite accurate, going as T^{-2}. A power-law curve fit of Eq. (B1) also produces an exponent of 2.03. Comparison of this scaling law is shown in Sec. III B.

[1] L. Aarons and S. Sundaresan, Powder Technol. **169**, 10 (2006).

[2] S. Luding and F. Alonso-Marroquin, Granular Matter **13**, 109 (2011).

[3] Y. Gu, S. Chialvo, and S. Sundaresan, Phys. Rev. E **90**, 032206 (2014).

[4] E. Irani, P. Chaudhuri, and C. Heussinger, Phys. Rev. Lett. **112**, 188303 (2014).

[5] E. Irani, P. Chaudhuri, and C. Heussinger, Phys. Rev. E **94**, 052608 (2016).

[6] C. S. Campbell, J. Fluid Mech. **465**, 261 (2002).

[7] R. Brewster, G. S. Grest, J. W. Landry, and A. J. Levine, Phys. Rev. E **72**, 061301 (2005).

[8] A. Singh, V. Magnanimo, K. Saitoh, and S. Luding, Phys. Rev. E **90**, 022202 (2014).

[9] D. Geldart, Powder Technol. **7**, 285 (1973).

[10] H. Kim and H. Arastoopour, Powder Technol. **122**, 83 (2002).

[11] R. Moreno-Atanasio, B. Xu, and M. Ghadiri, Chem. Eng. Sci. **62**, 184 (2007).

[12] T. Kobayashi, T. Tanaka, N. Shimada, and T. Kawaguchi, Powder Technol. **248**, 143 (2013).

[13] P. Liu, C. Q. LaMarche, K. M. Kellogg, and C. M. Hrenya, Chem. Eng. Sci. **145**, 266 (2016).

[14] A. Nienow, M. Edwards, and N. Harnby, *Mixing in the Process Industries: Mixing of Cohesive Powders*, 2nd ed. (Elsevier, Amsterdam, 1992).

[15] A. Castellanos, J. M. Valverde, A. T. Pérez, A. Ramos, and P. K. Watson, Phys. Rev. Lett. **82**, 1156 (1999).

[16] J. Colwell, S. Batiste, M. Horányi, S. Robertson, and S. Sture, Rev. Geophys. **45**, RG2006 (2007).

[17] A. Kulchitsky, J. Johnson, D. Reeves, and A. Wilkinson, in *Proceedings of the 14th ASCE Biennial International Conference on Engineering, Science, Construction, and Operations in Challenging Environments* (St. Louis, Missouri, 2014), pp. 485–494.

[18] A. DeCicco and C. Hartzell, in *Proceedings of the IEEE Aerospace Conference* (Big Sky, Montana, 2016).

[19] E. Murphy and S. Subramaniam, Powder Technol. **305**, 462 (2017).

[20] S. Takada, K. Saitoh, and H. Hayakawa, Phys. Rev. E **90**, 062207 (2014).

[21] N. Berger, E. Azéma, J.-F. Douce, and F. Radjai, Europhys. Lett. **112**, 64004 (2016).

[22] P. G. Rognon, J.-N. Roux, M. Naaim, and F. Chevoir, J. Fluid Mech. **596**, 21 (2008).

[23] E. Murphy and S. Subramaniam, Phys. Fluids **27**, 043301 (2015).

[24] P. Liu, K. Kellogg, C. LaMarche, and C. Hrenya, Chem. Eng. J. **324**, 380 (2017).

[25] J. Gaume, G. Chambon, and M. Naaim, Phys. Rev. E **84**, 051304 (2011).

[26] Q. Zhang and K. Kamrin, Phys. Rev. Lett. **118**, 058001 (2017).

[27] D. Berzi and J. T. Jenkins, Soft Matter **11**, 4799 (2015).

[28] D. Gollin, D. Berzi, and E. Bowman, Granular Matter **19**, 1564 (2017).

[29] GDR MiDi, Eur. Phys. J. E **14**, 341 (2004).

[30] S. Plimpton, J. Comput. Phys. **117**, 1 (1995).

[31] J. N. Israelichvili, *Intermolecular and Surface Forces: Revised Third Edition* (Academic Press, New York, 2011).

[32] D. Tabor, J. Colloid Interface Sci. **58**, 2 (1977).

[33] P. Cundall and O. Strack, Geotechnique **29**, 47 (1979).

[34] G. Kuwabara and K. Kono, Jpn. J. Appl. Phys. **26**, 1230 (1987).

[35] N. V. Brilliantov, F. Spahn, J.-M. Hertzsch, and T. Pöschel, Phys. Rev. E **53**, 5382 (1996).

[36] J. Schäfer, S. Dippel, and D. Wolf, J. Phys. I France **6**, 5 (1996).

[37] P. Jop, Y. Forterre, and O. Pouliquen, Nature (London) **441**, 727 (2006).

[38] B. Dahneke, J. Colloid Interface Sci. **51**, 58 (1975).

[39] A. Lees and S. Edwards, J. Phys. C **5**, 1921 (1972).

[40] S. Chialvo, J. Sun, and S. Sundaresan, Phys. Rev. E **85**, 021305 (2012).

[41] R. A. Bagnold, Proc. Roy. Soc. Lond. A **225**, 49 (1954).

[42] G. Lois, J. Blawzdziewicz, and C. S. O'Hern, Phys. Rev. Lett. **100**, 028001 (2008).

[43] K. Saitoh, S. Takada, and H. Hayakawa, Soft Matter **11**, 6371 (2015).

[44] See Supplemental Material at http://link.aps.org/supplemental/10.1103/PhysRevE.97.062902 for (i) animation of sheared systems for a frictionless systems with $\varepsilon = 0.9$ and Ha$_T$ = 0.01, which shows primarily binary collision events for systems with low cohesion, (ii) for animation of sheared systems for a frictionless systems with $\varepsilon = 0.9$ and Ha$_T$ = 3.4, which shows the large amount of fluctuations in the number of particles in a cluster near the transition, (iii) for animation of sheared systems for a frictionless systems with $\varepsilon = 0.9$ and Ha$_T$ = 16, which shows a large enduring percolating structure.

[45] S. Markutsya, R. O. Fox, and S. Subramaniam, Phys. Rev. E **89**, 062312 (2014).

[46] A. J. Liu and S. R. Nagel, Ann. Rev. Cond. Mat. Phys. **1**, 347 (2010).

[47] J. Sun and S. Sundaresan, J. Fluid Mech. **682**, 590 (2011).

[48] R. N. Chacko, R. Mari, S. M. Fielding, and M. E. Cates, arXiv:1707.01828.

[49] P. Haff, J. Fluid Mech. **134**, 401 (1983).

[50] K. M. Kellogg, P. Liu, C. Q. LaMarche, and C. M. Hrenya, J. Fluid Mech. **832**, 345 (2017).